Proceedings of ASME Turbo Expo 2011
GT2011
June 6-10, 2011, Vancouver, British Columbia, Canada

GT2011-45992

THE WHOLE ANNULUS COMPUTATIONS OF PARTICULATE FLOW AND EROSION IN AN AXIAL FAN

Hong Yang **Joan Boulanger**
Gas Turbine Laboratory, Institute for Aerospace Research
National Research Council Canada (NRC)
Ottawa, Ontario, Canada

ABSTRACT

Gas turbine engines operating in a hostile environment, polluted with sand or dust particles, are susceptible to the erosion damage, mostly at front axial fans and compressors. To accurately predict the erosion pattern and rate due to sand ingestion is one of the big challenges faced by the transportation and power industries. Maintenance costs are scrutinized and intensive research efforts are currently deployed in predictive life assessment tools to minimize the overhaul down time. The conventional prediction methods were usually based on steady-state simulations of gas-phase flows through a single blade passage per blade row to reduce computational cost. However, the multi-stage turbomachinery flows are intrinsically subject to unsteadiness, especially due to stator-rotor interactions which may affect sand particle trajectories even if a one-way coupling method is considered. Furthermore, an unsteady stator-rotor interaction asks for a whole-annulus model at great computational cost to avoid simplifications of geometries or flow physics. To study the effects of the stator-rotor interaction on sand particle trajectories and erosion, an axial fan with inlet guide vanes is investigated based on the whole annulus computations of both steady and unsteady gas-phase flows, each of which is then followed by a Lagrangian particle tracking step. A numerical algorithm for tracking particles driven by unsteady gas-phase flow is presented. The comparison of the numerical predictions with the experimental data confirms the validity and necessity of the unsteady CFD model in providing adequate predictions of sand erosion in the axial fan.

INTRODUCTION

Aero-engines and stationary gas turbines are often exposed to ingestion of sand or dust particles, causing the erosion of fan and compressor blades. To accurately predict the erosion pattern and rate due to sand ingestion is one of the big challenges faced by industry. Although Computational Fluid Dynamics (CFD) modeling is perceived as a cost effective avenue of the life assessment due to the prohibitive destruction of real engines for establishing life statistics, it still has difficulty dealing with sand particle rebound and erosion predictions. The reasons are twofold: (1) the generalities of experimental data and correlations restrict the CFD models; (2) the availability of advanced CFD techniques and computing power also restricts CFD models. Nevertheless, progressive experimental work during the last four decades has helped deepen understandings of particulate flows in turbomachinery as well as supplied empirical correlations for the numerical modeling on sand particle rebound and erosion. For instance, the experimental work of Ghenaiet, et al. [1-2] provides time-accurate experimental data about the sand erosion and performance degradation of a fan unit. Another example is the extensive experimental work by Tabakoff, Hamed and their co-workers, producing useful correlations for predicting particle rebound and erosion on compressors and turbines, e.g., [3-6].

The conventional CFD predictions for particulate flow and erosion were usually based on steady-state simulations of gas-phase flows through a single blade passage per blade row to reduce computational cost, e.g. [7-9]. However, the multi-stage turbomachinery flows are intrinsically subject to unsteadiness, especially due to stator-rotor interactions which may affect sand particle trajectories even if a one-way coupling method is under consideration. Although the unsteady flow in a compressor was considered in the sand erosion prediction by Suzuki et al. [10], they neglected rotor tip clearance, which may bring about uncertainties in capturing real flow physics involved in the studied compressor. On the other hand, pure gas-phase unsteady flow simulations themselves are still challenging for multi-stage turbomachines because of requirements of large computing power and high-fidelity interfacing techniques. One of the reasons for demanding such large computing power is the fact that in practical turbomachinery configurations blade counts are chosen such that periodicity (other than the whole annulus) does not occur, thus avoiding resonance. In order to minimize the size of the problem that needs to be computed, two types of approximations are introduced and they can be considered to be different variations of reduced-order models. The first approach involves rescaling the geometry including blade counts and chords such that periodicity assumptions hold in an azimuthal portion of the domain that is much smaller than the full annulus, e.g., [11]. A second alternative involves the use of the original geometry but compromises the fidelity of the time integration method, e.g., time spectral method [12], frequency-domain method [13] and harmonic balance method [14], etc. To avoid bias of blade loading and unsteadiness of reduced-order models, a direct model of real geometries in whole annulus would be a natural choice in spite of great computational cost [15].

To study the effects of the stator-rotor interaction on sand particle trajectories and erosion, an axial fan with inlet guide vanes from the Cranfield University [1-2] is investigated based on the whole annulus computations of both steady and unsteady gas-phase flows, each of which is then followed by a Lagrangian particle tracking step. The fan is a single-stage contra-whirl axial fan commonly used to provide ventilation to vital components in an aircraft. The available experimental data of this fan is used to validate an in-house CFD solver that is employed in this study. A numerical algorithm for tracking particles driven by unsteady gas-phase flow is presented, while a stochastic method to distribute particles into a downstream blade row is evaluated when coupled to steady gas-phase flow. The performance of these two models associated with steady and unsteady gas flow solutions is compared in terms of predicted changes in rotor tip clearance gap and rotor tip chord as well as rotor erosion patterns, revealing the necessity of the unsteady model to adequately predict sand erosion in the fan stage. To validate the implementation of particle rebound and erosion models in this study, an elbow test case from Eyler [16] is also computed and presented.

NUMERICAL FORMULATIONS FOR THE MULTI-PHASE FLOW SIMULATION

An Eulerian-Lagrangian approach has been developed to simulate the multi-phase flow involving gas and sand particles. It is assumed herein that the particle concentration in the flow field is small enough to ignore particle-particle collisions as well as the influence of sand particles on the gas-phase. Hence only one-way coupling of fluid-particle interactions is considered, assuming continuous gas phase and dispersed particle phase which are resolved with Eulerian and Lagrangian methods, respectively.

The gas-phase flow is assumed to be three-dimensional, compressible and turbulent, which is simulated with an in-house unstructured finite-volume based RANS solver INSECT [17-19]. To allow for large-scale computations, INSECT has been parallelized with non-blocking Message Passing Interface (MPI) techniques. An optimal load balance between various processors is achieved with help of PARMETIS [20]. In INSECT, the convective fluxes are discretized employing the 2nd-order accurate upwind scheme while the diffusive fluxes are formulated using the central differencing scheme. The discretized algebraic equation system is solved implicitly with the symmetric Gauss-Seidel (SGS) relaxation approach. To make turbulence closure, the Wilcox two-equation k-ω model [21] is applied and the stagnation-point anomaly is avoided by ensuring the realizability constraints of Durbin [22].

The treatment of boundary conditions is crucial for high-fidelity simulations of gas-phase flows, especially for the whole annulus turbomachinery configurations with multiple blade rows. The non-reflecting boundary conditions of Giles [23] are applied at inflow and outflow boundaries while no-slip boundary conditions are applied at solid walls in terms of low-Reynolds-number and wall-function formulations. At an interface between blade rows, for a steady-state simulation the mixing-plane model of Saxer and Giles [24] is applied in combination with the Dual Mesh Approach of Yang and Jiang [18] to enhance the accuracy on the unstructured grids, while for unsteady state simulation, a sliding mesh interface algorithm is applied based on the Conservative Zonal Approach of Yang et al. [11] [25].

Once the gas-phase flow simulation is completed, the fluid flow solution is provided for the particle phase which is then simulated by solving the following particle motion equation with the Lagrangian approach

$$\frac{d\vec{V}_P}{dt} = F_D\left(\vec{V}_F - \vec{V}_P\right) + \vec{g}\left(1 - \frac{\rho_F}{\rho_P}\right) + \vec{F}_A \tag{1}$$

$$\frac{d\vec{R}}{dt} = \vec{V}_P \tag{2}$$

In Eq. (1), $\vec{V}_F$ and $\vec{V}_P$ are fluid and particle velocity vectors, ρ_F and ρ_P are fluid and particle density, $\vec{g}$ is gravitational acceleration and $\vec{F}_A$ denotes an additional acceleration term. In Eq. (2), $\vec{R}$ is the location vector of a particle. The major component of the force acting on a particle is the drag, expressed as the first term on the RHS of Eq. (1), which is exerted on the particle by the fluid. F_D can be formulated as

$$F_D = 3\mu C_D Re_P / (4\rho_P\, d_P^2) \tag{3}$$

where d_P is particle diameter and C_D is the drag coefficient given by

$$C_D = \frac{24}{Re_P}\left(1 + 0.15 Re_P^{0.687}\right) \tag{4}$$

and the particle Reynolds number based on slip velocity between the particle and fluid, Re_P is defined by

$$Re_P = \rho_F\left|\vec{V}_P - \vec{V}_F\right| / \mu_F \tag{5}$$

The additional force term $\vec{F}_A$ may account for pressure gradients, added mass, as well as centrifugal and Coriolis effects. The centrifugal and Coriolis forces are important for turbomachinery applications in rotating coordinates, which is expressed as

$$\vec{F}_R = -[2\vec{\omega} \times \vec{V}_P + \vec{\omega} \times \left(\vec{\omega} \times \vec{R}\right)] \tag{6}$$

By fixing all force terms except the aerodynamic drag force at a specific time step, Eq. (1) can be solved analytically, which is then followed by either a forward Euler or a semianalytical integration of Eq. (2) to update the particle location $\vec{R}$. For turbomachinery applications, the motion of particles is usually computed in relative frame of reference for individual blade rows.

Usually a particle tracking in the one-way coupling approach is based on a steady flow field due to the fact that the sand erosion phenomenon needs a long period and the time scale is much longer than that of the flow field. However, for multi-stage turbomachinery applications, the stator-rotor interaction brings about strong unsteadiness which may considerably affect the particle motion. In addition, the steady-state flow solutions also cause uncertainties in modeling of particles across the blade row interface. Hence, it would be ideal to perform the time-accurate simulations for both gas phase and particle phase in the fan stage. To this end, a series of instantaneous flow fields are stored within one rotational period of the rotor, which are then used in the particle simulation. To minimize memory usage, only two instantaneous flow solutions at t_0 and $t_0+\Delta t$ are loaded into the memory for the particle trajectory computation, where t_0 is a time instant and Δt is the time interval for storing the flow solutions. When time $t_0+\Delta t$ is reached, the particle trajectory computation is halted until a new flow solution at $t_0+2\Delta t$ is loaded while the older flow solution at t_0 is removed from the memory. This process is repeated for all instantaneous flow solutions recorded within one rotational period.

For the particle boundary conditions, at an injection boundary the particles are seeded with specific concentration distribution along the boundary, while at a solid wall an adequate rebound model is applied. At an interface boundary between rotating and non-rotating blade rows, if the fluid flow is simulated in steady state with a mixing-plane model, the particles are distributed randomly along the circumferential direction when entering the neighboring blade row, while with a time-accurate fluid flow simulation, the particles are located accurately for the neighboring blade row based on their absolute coordinates at the interface. Furthermore, when the particles cross the blade row interface, their velocities need to be converted to the corresponding frame of reference used by the neighboring blade row.

In order to accurately predict the particle trajectories an appropriate particle rebound model needs to be used, predicting the particle-wall collision. Although extensive experimental work on particle rebound characteristics has been performed during the last four decades (e.g., [3-4, 26]), the resultant correlations of restitution ratios are highly empirical depending on the particle material, the surface material and the impact conditions. For the fan stage simulation, the rebound characteristics for Aluminum 2024 by Tabakoff and Hamed [4] are applied. After calculation of particle-wall collision, the erosion is predicted with an appropriate erosion model. The erosion models are also highly empirical, which should be verified in numerical modeling. For the fan stage simulation, the erosion model of Grant and Tabakoff [3] is applied, which provides the erosion ratio based on particle impingement velocity and direction as well as materials of the particles and the impinged walls. The validations of the rebound model and erosion model can be found in the next sections.

VALIDATION OF REBOUND AND EROSION MODELS

In order to validate the particle tracking and erosion modeling, the data of Eyler [16] was used as a test case. Eyler experimentally studied the erosion of an elbow installed in a pneumatic transport system. Seven data points were provided at each measurement location spanning the elbow in increments of 5 deg. Table 1 lists the fluid, sand particle and wall material properties used in the test. Following methods used in the literature [7, 27], the rebound model of Forder et al. [26] and the erosion model of Ahlert [28] are applied first. In addition, this test case is also used to evaluate the performance of some popular correlations for turbomachinery configurations from Tabakoff et al., i.e., the rebound model in [4] and erosion model in [3], respectively.

Table 1. TEST DATA FOR ELBOW EROSION STUDY [16].

Description	Value
Pipe diameter, D	41 mm
Turning radius ratio, r/D	3.25
Carrier fluid velocity	25.24 m/s
Carrier fluid	Air
Kinematic viscosity	1.512 x 10^{-5} m^2/s
Particle diameter	100 μm
Particle density	2560 kg/m^3
Particle-fluid mass ratio	0.75%
Pipe wall material	Carbon steel
Pipe wall density, ρ_w	7800 kg/m^3
Brinell harness, B	120

Figure 1 gives geometry layout and unstructured mesh for the elbow. The mesh consists of about 280,000 cells with non-dimensional wall distance y^+ less than 1 at near-wall cells.

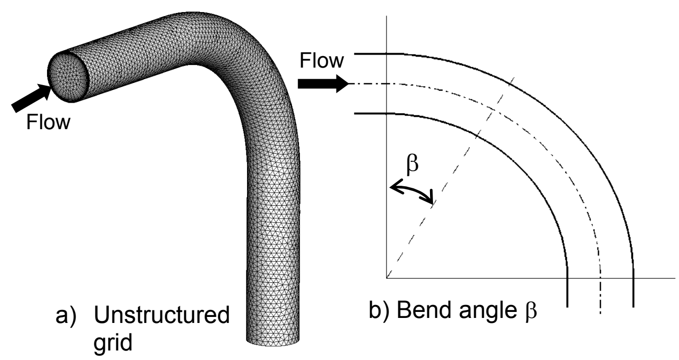

Figure 1. NUMERICAL MODEL OF AN ELBOW.

Figure 2 shows the local penetration distribution on elbow surface where all simulations use the same erosion model from Ahlert [28] but different rebound models, i.e., the one from Forder et al. [26] and the one from Tabakoff et al. [4] as well as elastic rebound. The local penetration rate $\dot{P}$ is calculated from

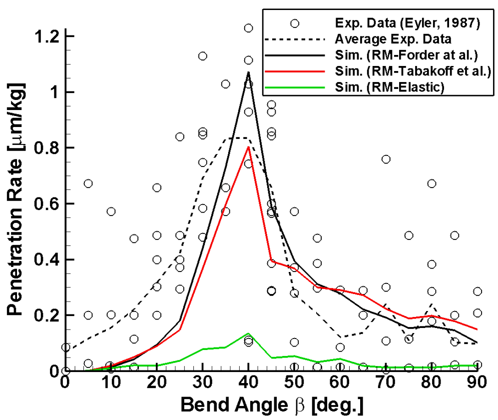

Figure 2. COMPARISON OF THE PREDICTED PENETRATION RATE WITH DATA OF EYLER[16] (all predictions use the same erosion model from Ahlert[28] but different rebound correlations).

the local erosion rate ε_L divided by pipe wall density and particle mass flow, which is actually the amount of wall thickness loss per unit mass of the particles. From Fig. 2, one may observe the variations of CFD predicted penetration rates with the rebound models from Forder et al. [26] and from Tabakoff et al. [4], are all in good agreement with those of experimental data, particularly the correct prediction of the maximum erosion location which is between 35 and 40 deg. of the bend angle. Nevertheless, as indicated in Fig. 2, the computation with elastic rebound seems to under-predict greatly the penetration rate in spite of its correct prediction on the maximum erosion location, and also the rebound model from Forder et al. [26] leads to better prediction at the locations from 20 to 35 deg. of the bend angle compared to use of the rebound model from Tabakoff et al. [4].

Next, the erosion model of Tabakoff et al. [3] is assessed in Fig. 3 where both CFD predictions apply the rebound model of Forder et al. [26]. From this figure, one may find that the

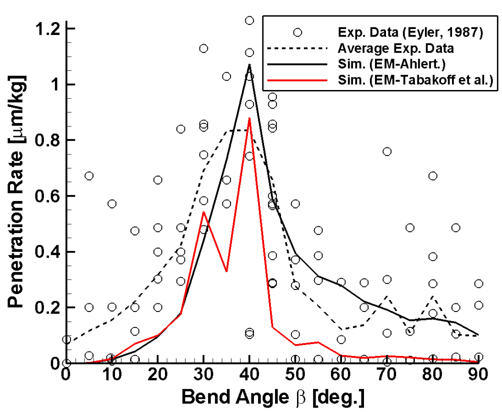

Figure 3. COMPARISON OF THE PREDICTED PENETRATION RATE WITH DATA OF EYLER[16] (both predictions use the rebound correlation from Forder et al.[26]).

erosion model of Tabakoff et al. [3] can capture the correct maximum erosion location. However, it under-predicts the erosion behind the maximum erosion location. Hence, the erosion model of Tabakoff, et al. [3], which was summarized from the experiments on turbomachinery configurations, may not be accurate for the elbow case. This means the erosion models are highly empirical so that they should be applied only for those configurations and materials upon which the models were built.

Figure 4 presents the computed contours of penetration rate

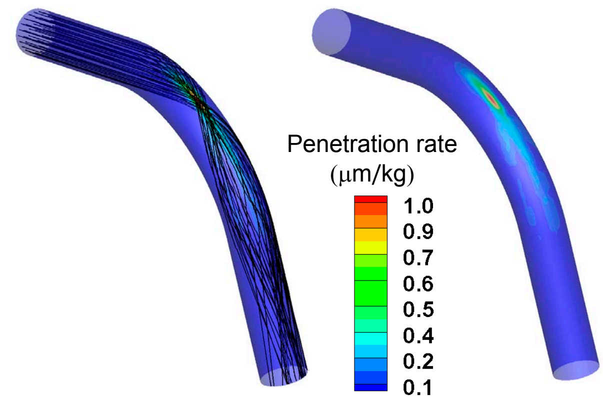

Figure 4. PENETRATION-RATE CONTOURS AND PARTICLE TRAJECTORIES IN THE ELBOW (with the erosion model of Ahlert[28] and the rebound model of Forder et al.[26]).

and particle trajectories obtained from the erosion model of Ahlert [28] and the rebound model of Forder et al. [26]. This figure clearly illustrates the tendency of particle impingements on the elbow pipe wall, leading to maximum penetration rate at the location between 35 and 40 deg. of the bend angle. Further validations on the erosion and rebound models will be presented in a later section for the case of the fan stage.

CFD MODELING OF A FAN STAGE IN FULL ANNULUS

An axial fan unit of Cranfield University [1-2] is simulated in both steady and unsteady flow states. The configuration and surface mesh for the fan unit are plotted in Fig. 5. The fan unit

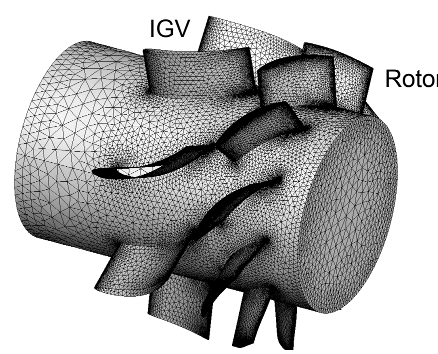

Figure 5. SURFACE MESH OF A FAN UNIT FROM CRANFIELD UNIVERSITY [1-2].

is a single-stage contra-whirl axial fan commonly used to provide ventilation to vital components in an aircraft. It consists of ten twisted C4 rotor blades and a set of seven C4 inlet guide vanes (IGVs). The geometrical parameters of this fan are shown in Table 2. The rotor blades made from cast aluminum were

Table 2. AXIAL FAN DESIGN PARAMETERS [1].

Description	Value
Shroud diameter	170.02 *mm*
Rotor root diameter	110 *mm*
Rotor tip diameter	169.37 *mm*
Rotor tip chord	45.57 mm
Rotor root chord	43.08 *mm*
Rotor space-chord ratio	0.991
Rotor hub-tip ratio	0.647
Rotor tip stagger angle	55.25^0
Rotor root stagger angle	48^0
Rotor root inlet blade angle	67.72^0
Rotor tip inlet blade angle	72.69^0
IGV chord	57.14 *mm*
IGV stagger angle	27.36^0
IGV inlet blade angle	0^0
IGV-rotor axial spacing	15 *mm*
Flow coefficient	0.5
Pressure rise coefficient	0.4

used in the experiments by Ghenaiet et al. [1-2]. The fan was driven by a three-phase 400 Hz electric motor at a nominal speed of 11300 rpm.

The fan unit has been modeled as a whole annulus to avoid simplifying the geometry or physics when dealing with unsteady stator-rotor interactions. In this study, a number of hybrid unstructured grids were generated, ranging from 2 million to 4 million cells which all require use of wall functions to tackle turbulent boundary layers. The grid independency test shows that a hybrid unstructured grid with 2.809M cells can achieve similar global results (such as adiabatic efficiency and pressure ratio) to those computed on the finer grid with 4M cells. Hence, to reduce computational cost, the grid with 2.809M cells is used in this study. It results in the non-dimensional wall distance y^+ in the range of 16 to 62 near all solid walls. Figure 6 gives details of mesh distribution around the blades.

At first, the steady gas-phase flows through the fan stage are simulated at various mass flow rates to compare with the experimental data of Ghenaiet [2], Fig. 7. To demonstrate the performance of unsteady state simulation, the time-averaged result at mass flow rate 0.8 kg/s is also plotted in Fig. 7. As indicated by Fig. 7, the computed adiabatic efficiency and pressure rise coefficient generally agree well with the measurement data if considering the uncertainties of the measurement expressed as error bars in the figure. Particularly near the design point with about 0.785 kg/s mass flow, the measurement and CFD prediction are found to match closely. This result gives confidence on the CFD solver. Furthermore, one may notice from Fig. 7 that the time average of the

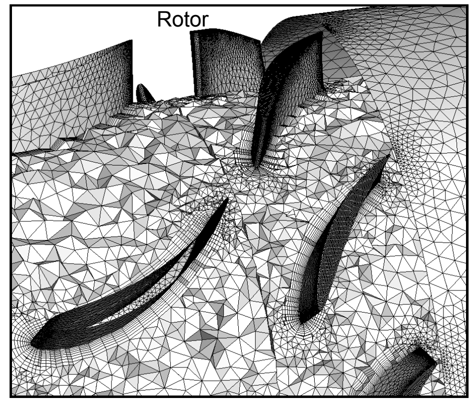

Figure 6. UNSTRUCTURED MESH FOR THE FAN UNIT (2.809M cells).

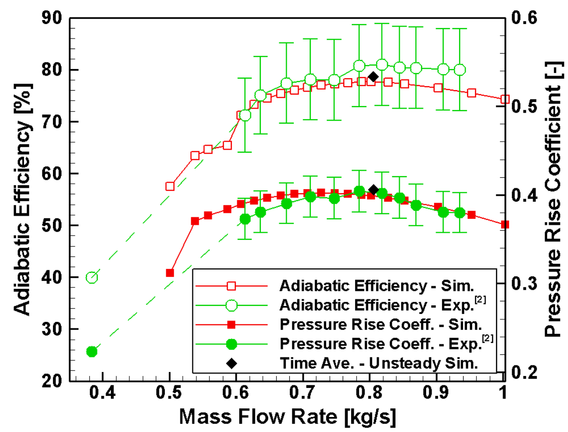

Figure 7. COMPARISON OF PERFORMANCE MAP FOR THE AXIAL FAN STAGE AT ROTATIONAL SPEED 11300 RPM.

unsteady solution leads to closer agreement with the experiment than the steady solution at 0.8 kg/s mass flow.

With the steady state solution near the design point as initial flow field, a time-accurate simulation of the fan stage is conducted. The time-averaged flow properties at inlet and outlet boundaries are defined based on the data given by Ghenaiet et al. [1] with the ambient pressure and temperature of 100 kpa and 288 k, respectively. The inlet velocity and yaw angle in the radial direction are specified according to Fig. 10 in Ref. [1] where the velocity and yaw angle distribute along the radius in range of [44.7, 54.5] m/s and [87.4, 94.7] deg., respectively. In addition, the back pressure at the outlet is specified to achieve a time-averaged mass flow rate 0.8 kg/s.

For the time-accurate simulation, Figure 8 presents the time history of the computed mass flow rates at inlet, outlet and interface boundaries. The averaged mass flow rate in Fig. 8a is calculated by an ensemble average of mass flow rate over all time instants within one rotational period and the instantaneous mass flow rate is plotted in Fig. 8b for the periods 19 and 20. Figure 8a indicates that the unsteady computation spends about 15 rotational periods to reach temporal periodicity with constant time-averaged mass flow rates at all monitoring

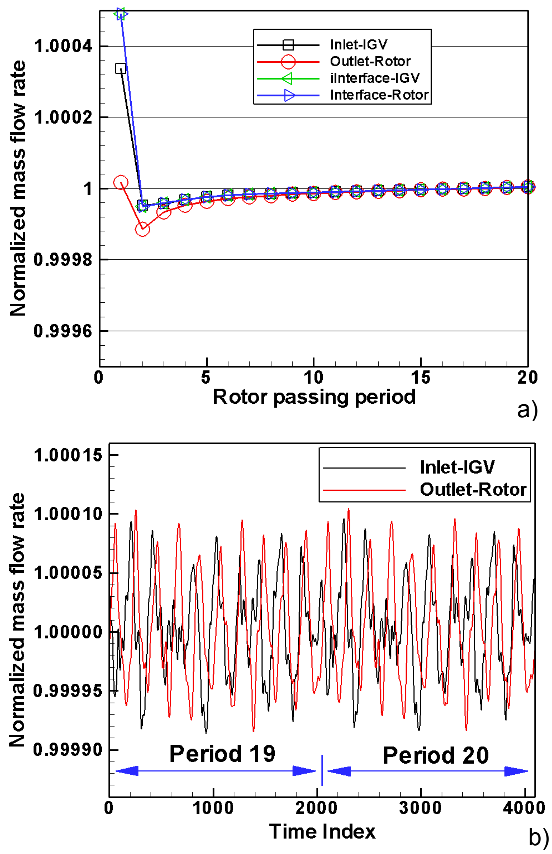

Figure 8. COMPUTING HISTORY OF THE MASS FLOW RATE: a) averaged mass flow rate vs. rotational periods; b) instantaneous mass flow rate for the last two periods.

boundaries, while Fig. 8b shows instantaneous change of mass flow rate at convergence, from which one can observe the temporal periodicity between the two rotational periods in spite of fluctuated disturbances during one turn of the full annulus.

In Fig. 9, a fast Fourier transform (FFT) analysis of the computed mass flow rate at the sliding mesh interface reveals all important disturbance frequencies associated with the unsteady IGV-rotor interactions. The rotor rotating frequency is denoted as f_1 in this figure, while the rotor blade passing frequency and IGV passing frequency are denoted as $f_{BPF\text{-}rotor}$ and $f_{BPF\text{-}IGV}$, respectively. From this figure one may find several harmonics associated with the IGV-rotor interaction, among which the first harmonics of $f_{BPF\text{-}rotor}$ and $f_{BPF\text{-}IGV}$ show distinguished magnitudes compared to the rest of the harmonics. For a grid cell in the rotating coordinates with rotor blades, it experiences unsteady disturbance from the stationary IGVs. The axial velocity at such a grid cell is analyzed in Fig. 10, from which one may observe a few clearly resolved harmonics which are integer multiples of the IGV's BPF. Figures 9 and 10 can verify the quality of the unsteady flow simulation in this study.

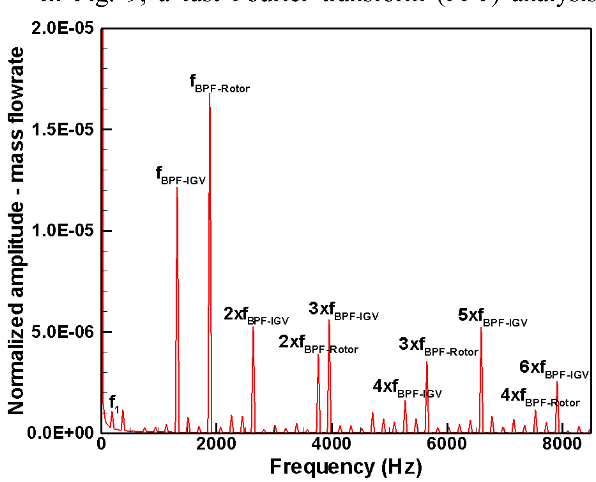

Figure 9. FFT SPECTRUM OF UNSTEADY MASS FLOW RATE AT THE SLIDING MESH INTERFACE.

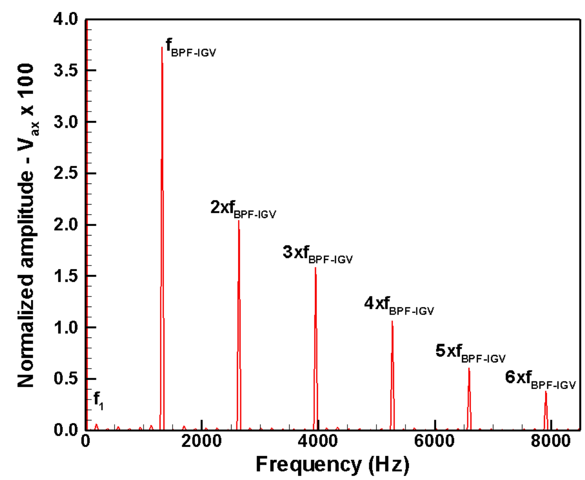

Figure 10. FFT SPECTRUM OF AXIAL VELOCITY AT A GRID CELL IN FRONT OF A ROTOR BLADE IN THE RELATIVE FRAME OF REFERENCE.

To show unsteady interactions between the rotor blades and IGVs, Figure 11 presents the instantaneous contours of turbulent viscosity at the mid-span, corresponding to several scenarios in sequence with a time interval of $T_r/32$, where T_r is the rotational period. For clarity of rotor movement, a reference rotor blade is marked with symbol b_0. From this figure one may observe that the wakes from IGVs are periodically chopped by the moving rotor blades so that they may interfere with the flow along rotor-blade surfaces, and eventually they mix with the downstream wakes stemmed from rotor blades.

PARTICLE TRACKING AND EROSION PREDICTION FOR THE FAN STAGE

The so-called global injection test by Ghenaiet et al. [1] has been numerically simulated with the above whole annulus modeling. The numerical simulation uses the flow conditions as well as the particle size and concentration profiles measured by the experiment [1-2]. Figure 12 gives the particle size distribution for silica sand (0-1000μm) which is commonly used for gas turbine erosion testing according to US Army

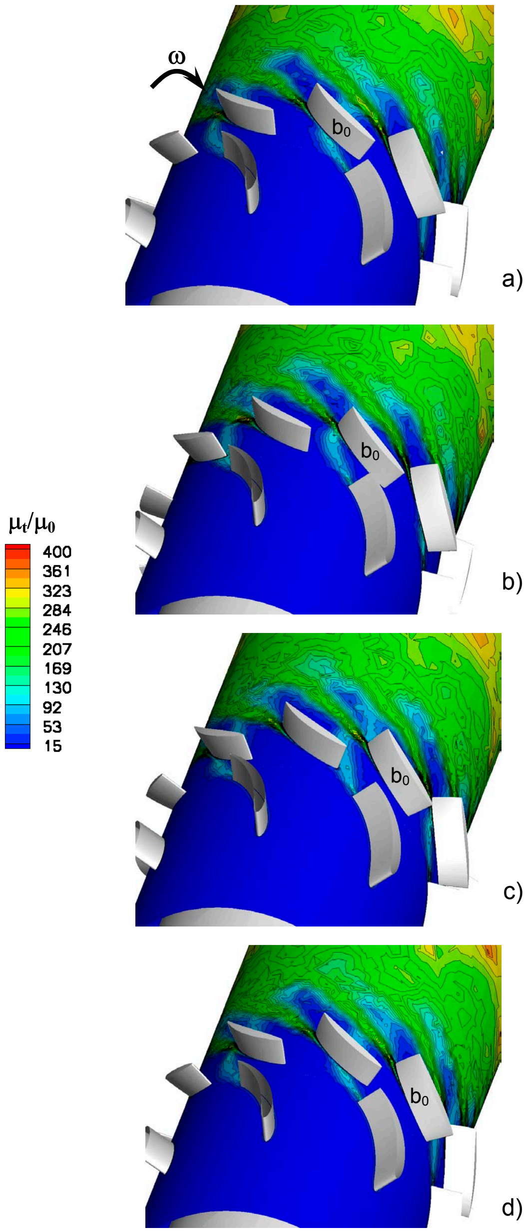

Figure 11. INSTANTANEOUS TURBULENT VISCOSITY CONTOURS AT THE MID-SPAN: a) $t = t_0$; b) $t = t_0 + T_r/32$; c) $t = t_0 + 2T_r/32$; d) $t = t_0 + 3T_r/32$.

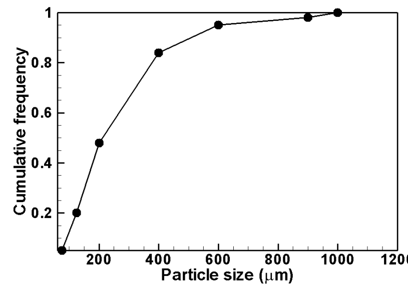

Figure 12. THE CUMULATIVE FREQUENCY FOR MIL-E5007E (0-1000μm) SAND PARTICLES.

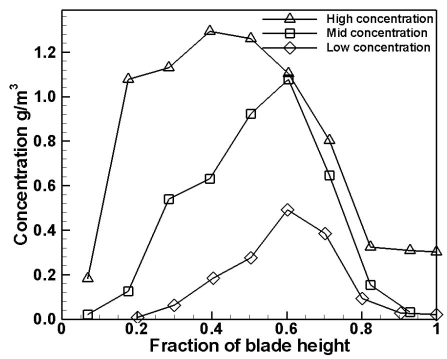

Figure 13. CONCENTRATION PROFILES MEASURED AT 50 MM FROM THE IGV[1].

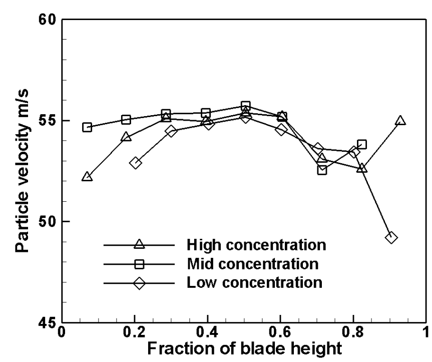

Figure 14. THE PARTICLE VELOCITY MEASURED AT 50 MM FROM THE IGV[1].

specifications MIL-E 5007 E [29]. Figures 13 and 14 give the particle concentration and velocity profiles respectively at the measuring plane which is 50 mm in front of IGV. Three levels of particle concentration are considered here, namely low concentration, mid concentration and high concentration. The particles are seeded along the radius of the inlet boundary according to the distributions specified in these two figures. However, in the circumferential direction, the particles are seeded randomly to have statistically sound distributions of the particles.

Usually only a finite number of particles is used in the erosion simulation such that a computed particle may represent a group of real particles to assure the actual particle mass flow rate. However, the number of computed particles should be big enough to represent realistic particle distribution and to reduce scatter in the erosion predictions. Hence, the independency test for the number of computed particles is first performed, Fig. 15. Figure 15 shows that 300,000 computed particles would be necessary for the fan-stage erosion prediction. A further increase in the number of computed particles to, say 400,000, does not change much the computed average erosion rates on both rotor and IGV blades as indicated by this figure.

Both steady and unsteady fluid flow solutions are provided for the erosion predictions. If the steady flow field is used for the particle tracking, the particles are distributed randomly in

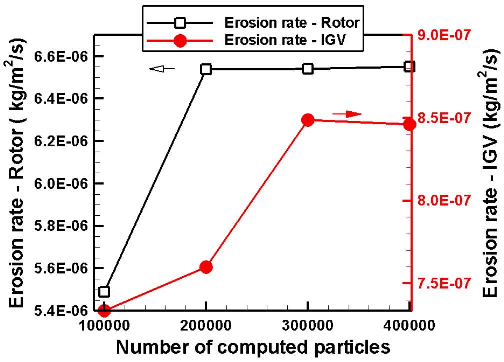

Figure 15. THE COMPUTED AVERAGE EROSION RATES ON THE ROTOR AND IGV BLADES VERSUS NUMBERS OF COMPUTED PARTICLES (mid concentration).

the circumferential direction when they are crossing the interface to enter into the neighboring blade row. With use of unsteady flow solutions, the particles are tracked continuously across the interface in a time-accurate manner. These two models are denoted as "Sim.(S)" and "Sim.(U)", respectively. Figures 16 and 17 compare the predicted changes in tip clearance gap and tip chord with the experimental data of

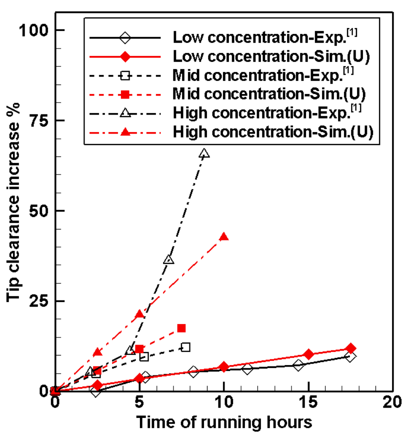

a)

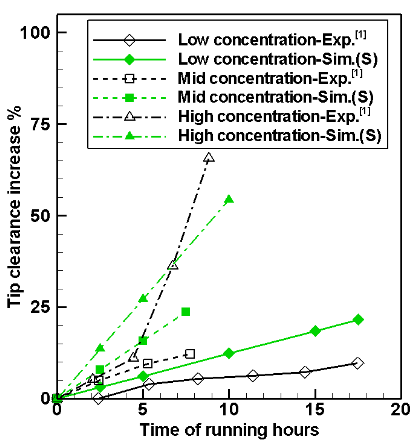

b)

Figure 16. TIP CLEARANCE INCREASE WITH RUNNING TIME: a) unsteady model; b) steady model.

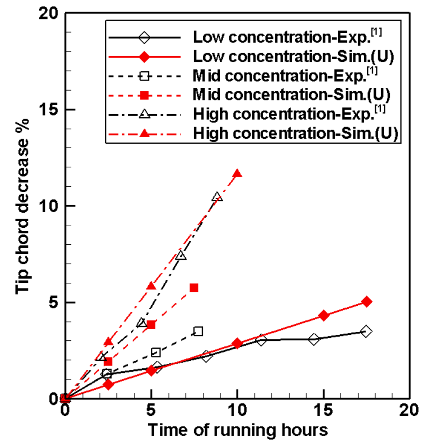

a)

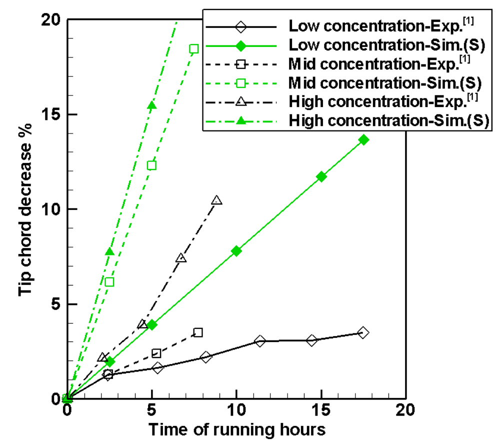

b)

Figure 17. TIP CHORD REDUCTION WITH RUNNING TIME: a) unsteady model; b) steady model).

Ghenaiet et al. [1]. The predicted changes in tip clearance gap and tip chord are calculated by multiplying the predicted erosion rate in units of thickness loss per unit time on the relevant wall to the running time. Therefore, the predicted changes are depicted in linear variation with the running time. Nevertheless, the CFD predictions with the unsteady model can achieve similar results or at least in same order of magnitude as the experiment for most of the points shown in Figs. 16 and 17. On the other hand, the CFD predictions with the steady model generally over-predict the geometry changes, leading to large discrepancies with the measurement data. To quantify the difference with the measurement data, Tables 3 provides relative differences between the predicted and measured changes in rotor tip clearance gap and tip chord at several running hours as well as their averages. This table can further confirm the validity of the unsteady model. For instance, at the low concentration with the unsteady model, the predicted changes in rotor tip clearance gap and tip chord are only 2.3% and 7.0% different than the measurement data at running time of 5 hours, while the averaged differences over the three time instants are about 15.5% and 16.8%, respectively. However, the CFD predictions with the steady model greatly over-predict the

Table 3. RELATIVE DIFFERENCES WITH EXPERIMENTAL DATA: a) low concentration; b) mid concentration; c) high concentration.

a)

	Tip-gap increase (%)				Tip-chord decrease (%)			
	Running hours			Average	Running hours			Average
	5.0	10.0	15.0		5.0	10.0	15.0	
Sim.(U)	2.3	13.1	30.9	15.5	7.0	7.0	36.5	16.8
Sim.(S)	77.8	105.8	138.3	107.3	152.8	191.0	271.1	205.0

b)

	Tip-gap increase (%)				Tip-chord decrease (%)			
	Running hours			Average	Running hours			Average
	2.5	5.0	7.5		2.5	5.0	7.5	
Sim.(U)	17.1	29.2	46.7	31.0	44.2	68.0	69.9	60.7
Sim.(S)	58.2	74.6	98.1	77.0	363.8	440.4	446.7	417.0

c)

	Tip-gap increase (%)				Tip-chord decrease (%)			
	Running hours			Average	Running hours			Average
	2.5	5.0	8.8		2.5	5.0	8.8	
Sim.(U)	68.5	23.3	42.9	44.9	13.3	32.3	1.21	15.6
Sim.(S)	114.8	57.2	27.2	66.4	200.1	250.3	161.7	204.1

changes in rotor tip gap clearance and tip chord by about 107.3% and 205.0% as shown in Table 3a.

Figure 18 compares the predicted and measured erosion patterns on the rotor blade pressure side at the high sand concentration. From this figure, one may observe that the CFD prediction with the unsteady model also captures the net leading edge erosion extending to the entire tip corner as well as a strip near the tip along which many particles impact the pressure side of rotor blades. As a comparison, the CFD prediction with the steady model is also provided in Fig. 19 which shows over-predicted erosion rate on rotor-blade pressure side as well as the leading and trailing edges.

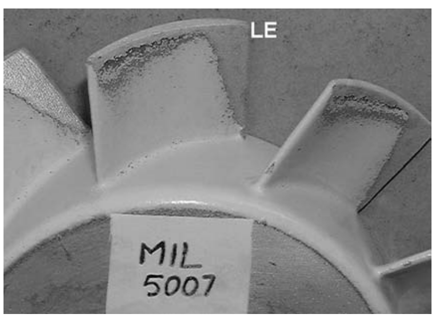

a)

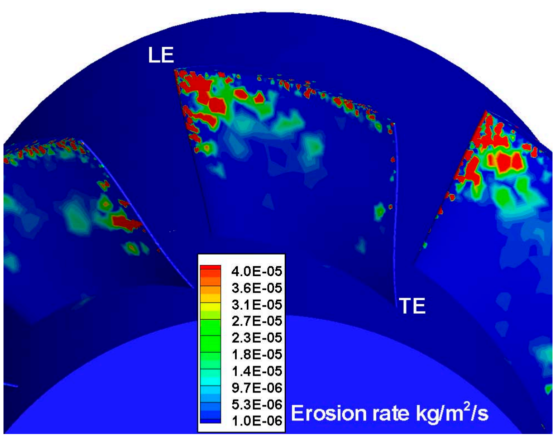

b)

Figure 18. COMPARISON OF EROSION PATTERN ON ROTOR BLADES: a) photograph of erosion by experiment[1]; b) erosion rate predicted with the unsteady model (high concentration).

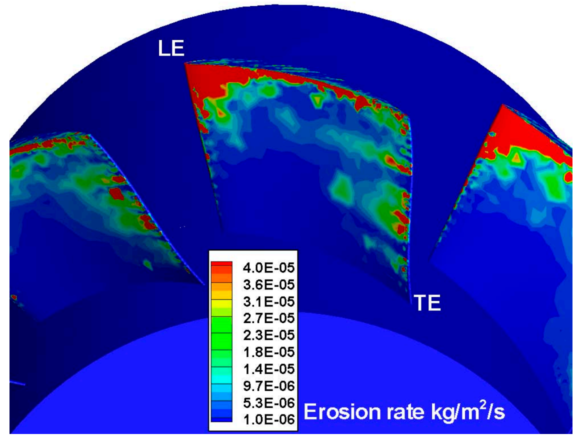

Figure 19. CONTOURS OF EROSION RATE ON ROTOR BLADES BY THE STEADY MODEL (high concentration).

Figure 20 presents some particle path-lines in the absolute frame of reference, which are calculated with the unsteady model. For clarity, the casing wall is removed from the view. The path-lines can demonstrate how the particles enter into rotor blade passages and how they impact with rotor, IGV and casing walls. Among these particles, an interesting particle motion is identified and shown in Fig. 21: first it impinges and

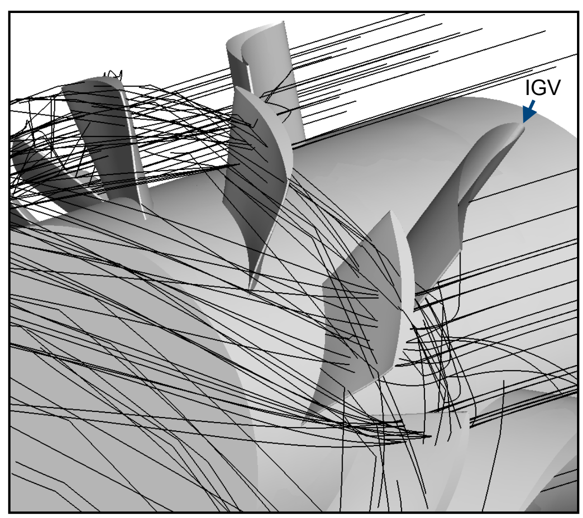

Figure 20. PARTICLE TRAJECTORIES IN ABSOLUTE FRAME OF REFERENCE AT THE MID CONCENTRATION WITH THE UNSTEADY MODEL (the casing wall is removed for clarity).

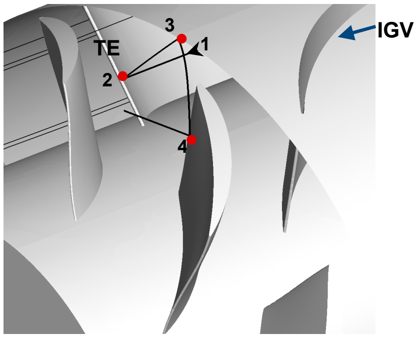

Figure 21. A PARTICLE PATH-LINE TO DEMONSTRATE THE PARTICLE IMPINGEMENT ONTO THE CASING AND ROTOR PRESSURE SURFACE, WITH THE UNSTEADY MODEL (impingement points are denoted by red spots).

rebounds on the trailing edge of IGV. Then it hits the casing wall and reflects into a rotor blade passage. Afterwards it impacts the rotor-blade pressure side and rebounds toward a neighbor blade. Hence, these computational results can help understand the mechanisms of particle motion and particle-wall collision associated with the fan unit. This unique insight into particle trajectory can be only obtained with the full transient simulation.

CONCLUSIONS

The whole annulus computations of particulate flow and erosion have been performed for an axial fan stage in both steady and unsteady states of gas phase. The comparisons of the CFD predictions with the experimental data have verified the validity and necessity of the unsteady CFD model.

The unsteady flow simulation for the fan unit in whole annulus is able to capture all important unsteadiness due to IGV-rotor interactions, which can provide physically-sound and time-accurate flow fields for the follow-up particle-phase simulation with the Lagrangian approach. The unsteady model can also avoid the uncertainties in distributing particles into neighboring blade rows, which are usually suffered by nearly all steady CFD models, no matter whether frozen rotor or circumferentially random distribution methods were used.

The implementation of some popular particle rebound and erosion models have been validated through the test cases of the elbow and the fan unit in this study. The computed results have shown that these empirical correlations are important for accurate particle tracking and erosion predictions. To improve the prediction accuracy, more accurate particle rebound and erosion models in a wider operating range would be desired.

In the future, the unsteady model presented in this study will be extended to evaluate compressor performance degradation due to the geometry changes caused by sand erosion.

ACKNOWLEDGMENTS

The authors wish to acknowledge the support of the Department of National Defence (DND). Also appreciation is expressed to Dr. L.Y. Jiang and Mr. J. Bird for project coordination.

NOMENCLATURE

BPF	Blade passing frequency
EM	Erosion model
M	Million
$\dot{m}$	Mass flow rate
$\dot{P}$	Local penetration rate, $\varepsilon_L/\rho_W\,\dot{m}_{Pt}$ $(\mu m/kg)$
$\vec{R}$	Location vector, $x\vec{\imath}+y\vec{\jmath}+z\vec{k}$
RANS	Reynolds-averaged Navier-Stokes equations
RHS	Right hand side
RM	Rebound model
Sim.(S)	Simulation with steady flow field
Sim.(U)	Simulation with unsteady flow field
t	Time
T_r	Rotational period
$\vec{V}$	Velocity vector
y^+	Non-dimensional wall distance, $\Delta y \cdot u_\tau / \nu$
ε_L	Local erosion rate (kg/m^2/s)
μ	Molecular viscosity
μ_t	Turbulent viscosity
ρ	Density
$\vec{\omega}$	Angular velocity vector

Subscripts

F	Fluid
P	Sand particles
W	Wall

REFERENCES

[1] Ghenaiet, A., Tan, S.C., and Elder R.L., 2004, "Experimental Investigation of Axial Fan Erosion and Performance Degradation", *Proc. Instn Mech. Engrs*, *Part A: J. Power and Energy*, Vol. **218**, pp. 437-450.

[2] Ghenaiet, A., 2001, "Turbomachinery Performance Degradation due to Erosion Effect", Ph.D. thesis, Cranfield University, UK.

[3] Grant, G. and Tabakoff, W., 1975, "Erosion Prediction in Turbomachinery Resulting from Environmental Solid Particles", *J. Aircraft*, Vol.**12**, pp. 471-478.

[4] Tabakoff, W. and Hamed, A., 1996, "Effect of Target Materials on the Particle Restitution Characteristics for Turbomachinery Application", *J. Propulsion and Power*, Vol. **12**, pp. 260-266.

[5] Tabakoff, W., 1984, "Review-Turbomachinery Performance Deterioration Exposed to Solid Particulates Environment", *ASME J. Fluids Eng.*, Vol. **106**, pp. 125-134.

[6] Hamed, A., Tabakoff, W., Rivir, R.B., et al., 2005, "Turbine Blade Surface Deterioration by Erosion", *ASME J. Turbomach.*, Vol. **127**, pp. 445-452.

[7] Dai, L., Yu, M., and Dai, Y., 2007, "Nozzle Passage Aerodynamics Design to Reduce Solid Particle Erosion of a Supercritical Steam Turbine Control Stage", *Wear*, Vol. **262**, pp. 104-111.

[8] Ghenaiet, A., Tan, S.C., and Elder, R.L., 2005, "Prediction of an Axial Turbomachine Performance Degradation due to Sand Ingestion", *Proc. IMechE*, Vol. **219**, *Part A: J. Power and Energy*, pp. 273-287.

[9] Suzuki, M. and Yamamoto., M., 2010, "Numerical Simulation of Sand Erosion in a Transonic Compressor Rotor", *ASME Turbo Expo 2010*, GT2010-23593, Glasgow, UK.

[10] Suzuki, M., Inaba, K., and Yamamoto. M., 2008, "Numerical Simulation of Sand Erosion Phenomena in Rotor/Stator Interaction of Compressor", *J. Thermal Science*, Vol. **17**, pp. 125-133.

[11] Yang, H., Nuernberger, D., and Weber, A., 2002, "A Conservative Zonal Approach with Application to Unsteady Turbomachinery Flows", *DGLR Jahrestagung*, Stuttgart, Sept. 23-26.

[12] Van der Weide, E., Gopinath, A., and Jameson, A., 2005, "Turbomachinery Applications with the Time Spectral Method", *AIAA Paper 05-4905*.

[13] Hall, K.C., Clark, W.S., and Lorence, C.B., 1994, "A Linearized Euler Analysis of Unsteady Transonic Flows in Turbomachinery", *ASME J. Turbomach.*, Vol. **116,** pp. 477-488.

[14] Ekici, K. and Hall, K.C., 2006, "Nonlinear Analysis of Unsteady Flows in Multistage Turbomachines Using the Harmonic Balance Technique", *AIAA paper 06-0422*.

[15] Roeber, T., Kuegeler, E., and Weber, A., 2010, "Investigation of Unsteady Flow Effects in an Axial Compressor Based on Whole Annulus Computations", *ASME Turbo Expo 2010*, GT2010-23522, Glasgow, UK.

[16] Eyler, R., 1987, "Design and Analysis of a Pneumatic Flow Loop", M.S. thesis, West Virginia University, Morgantown, MV.

[17] Yang, H. and Jiang, L.Y., 2009, "Development of High-Fidelity CFD Solvers toward Building Virtual Engine Capabilities for Gas Turbines", *17th Annual Conference of CFD Society of Canada*, Kanata, Ontario, May 3-5, 2009.

[18] Yang, H. and Jiang, L.Y., 2010, "A Dual Mesh Approach to Enhance Accuracy of the Boundary Conditions for Unstructured Grid Modeling of Turbomachinery Flows", *ASME Turbo Expo 2010*, GT2010-23390, Glasgow, UK.

[19] Yang, H., 2010, "Assessment of Parallel Performance of a 3D Unstructured CFD Solver on Linux Cluster with Multi-Core Processors", *18th Annual Conference of the CFD Society of Canada*, London, Ontario, May 17-19, 2010.

[20] Karypis, G., Schloegel, K., and Kumar, V., 2003, "PARMETIS – Parallel Graph Partitioning and Sparse Matrix Ordering Library, Version 3.1", University of Minnesota.

[21] Wilcox, D.C., 1998, "Turbulence Modelling for CFD", 2nd ed., DCW Industries, Anaheim.

[22] Durbin, P.A., 1996, "On the *k*-3 Stagnation Point Anomaly", *Int. J. Heat Fluid Flow*, Vol. **17**, pp. 89-90.

[23] Giles, M. B., 1990, "Nonreflecting Boundary Conditions for Euler Conditions," *AIAA J.*, Vol. **28**, pp. 2050-2058.

[24] Saxer, A.P. and Giles, M.B., 1993, "Quasi-Three-Dimensional Nonreflecting Boundary Conditions for Euler Equations Calculations", *J. Propulsion and Power*, Vol. **9**, pp. 263-271.

[25] Yang, H., Nuernberger, D., Nicke, E., and Weber, A., 2003, "Numerical Investigation of Casing Treatment Mechanisms with a Conservative Mixed-Cell Approach", *ASME Turbo Expo 2003,* GT-2003-38483, Atlanta, Georgia.

[26] Forder A., Thew M., and Harrison, D., 1988, "Numerical Investigation of Solid Particle Erosion Experienced within Oilfield Control Valves", *Wear*, Vol. **216**, pp.184-193.

[27] Edwards, K.J., McLaury B.S., and Shirazi, S.A., 2001, "Modeling Solid Particle Erosion in Elbows and Plugged Tees", *ASME J. Energy Resour. Technol.*, Vol. **123**, pp. 277-284.

[28] Ahlert, K., 1994, "Effects of Particle Impingement Angle and Surface Wetting on Solid Particle Erosion of AISI 1018 Steel", M.S. thesis, Department of Mechanical Engineering, The University of Tulsa, Tulsa, OK.

[29] Edwards, R.V. and Rouse, P.L., 1994, "US Army Rotorcraft Turboshaft Engines Sand and Dust Erosion Considerations", *AGARD*, Erosion, Corrosion and Foreign Object Damage Effects in Gas Turbines, Quebec, Canada.

